Cryogenic x-ray diffraction microscopy utilizing high-pressure cryopreservation

Enju Lima,[1,*] Yuriy Chushkin,[2] Peter van der Linden,[2] Chae Un Kim,[3,4] Federico Zontone,[2] Philippe Carpentier,[2] Sol M. Gruner,[4,5] and Petra Pernot[2]

[1]*Photon Sciences, Brookhaven National Laboratory, Upton, NY, 11973 USA*

[2]*European Synchrotron Radiation Facility, 71, avenue des Martyrs 38000 Grenoble, France*

[3]*Department of Physics, Ulsan National Institute of Science and Technology, Ulsan 689-798, Republic of Korea*

[4]*Cornell High Energy Synchrotron Source, Ithaca, NY 14853 USA*

[5]*Department of Physics, Cornell University, Ithaca, NY 14853 USA*

(Received 29 July 2014; published 15 October 2014)

We present cryo x-ray diffraction microscopy of high-pressure-cryofixed bacteria and report high-convergence imaging with multiple image reconstructions. Hydrated *D. radiodurans* cells were cryofixed at 200 MPa pressure into ∼10-μm-thick water layers and their unstained, hydrated cellular environments were imaged by phasing diffraction patterns, reaching sub-30-nm resolutions with hard x-rays. Comparisons were made with conventional ambient-pressure-cryofixed samples, with respect to both coherent small-angle x-ray scattering and the image reconstruction. The results show a correlation between the level of background ice signal and phasing convergence, suggesting that phasing difficulties with frozen-hydrated specimens may be caused by high-background ice scattering.

DOI: 10.1103/PhysRevE.90.042713 PACS number(s): 87.59.−e, 87.80.−y, 87.16.−b

I. INTRODUCTION

The high penetration power of x-rays has long been valued for noninvasive imaging of microns-to-centimeter thick biological samples in their entirety [1,2]. The short wavelength of x-rays, combined with the ability to detect trace elements or minute density variations, further enables imaging of unlabeled specimens beyond the resolution of optical microscopy [3,4]. As we progress towards nanometer scale resolution, structural damage due to ionizing radiation becomes the major limiting factor with biological specimens [5]. By dispensing with low-efficiency x-ray optics, x-ray diffraction microscopy (XDM) delivers an efficient radiation dose and offers high-resolution imaging capabilities by allowing an achievable resolution up to the maximum scattering angle of a sample [6]. These advantages in combination with cryoprotection open a door for XDM to deliver 5 to 10 nm resolution imaging of thick specimens in their unmodified "wet" conditions [7,8], thus presenting a new capability in life science.

XDM computationally recovers the lost phase information in the x-ray diffraction pattern of a sample by means of an iterative phasing algorithm [9,10]. Fourier inversion of such a phased diffraction pattern produces an image of a sample in x-ray absorption or phase contrast (or both). With the high coherent x-ray flux available at modern synchrotron sources, the method has rapidly developed [11–18] since the first feasibility demonstration with a test object [19]. While the imaging of radiation-hardy samples, such as nanocrystals, has steadily expanded [13–15], early work in cellular imaging had been limited to stained or dried specimens [11,12,16]. The need to image hydrated specimens under conditions close to their living states is apparent; however, wet specimens are inevitably subject to radiation damage and require cryoprotection in high-resolution imaging [20,21]. Ongoing efforts have resulted in the demonstration of cryo XDM in imaging frozen-hydrated bacteria and yeast [22,23]. Yet poor imaging performance due to the low-phasing convergence of x-ray diffraction from frozen-hydrated specimens has continued to be a major challenge. This limitation needs to be overcome in order to advance cryo XDM for wide applications in biological imaging and to reach the expected 5 to 10 nm resolutions.

In this paper, we demonstrate high-convergence imaging of cryo XDM across multiple image reconstructions of frozen-hydrated bacteria by utilizing high-pressure cryopreservation. In the first application of high-pressure cryopreservation to whole cellular imaging in cryo-XDM, we demonstrate cryofixing *D. radiodurans* bacteria at a pressure of 200 MPa into ∼10-μm-thick water layers. A comparison study of cryo XDM using high-pressure and ambient-pressure cryofixed *D. radiodurans* was carried out to find the possible causes of the phasing difficulties with frozen-hydrated specimens. The results showed enhanced phasing convergence with high-pressure-cryofixed specimens and their reconstructions revealed unstained, hydrated cellular environments at sub-30 nm resolution in two dimensions. Although there is a general notion that the weak x-ray diffraction from unstained frozen-hydrated biological specimens might be accountable for earlier phasing difficulties, our results show otherwise. The observed correlation between local ice conditions and phasing convergence suggests that high-background ice scattering may be responsible for poor convergence in frozen-hydrated imaging.

II. METHODS AND RESULTS

Imaging in life science aims to portray biological structures under conditions as close as possible to their native, functional states. Preserving and imaging samples in a frozen-hydrated state avoids the need for many other sample preparations which could introduce artifacts, such as chemical fixation, staining, or dehydration. Immobilizing cellular structures into an ice matrix further mitigates radiation damage artifacts such as mass loss [20]. Since water is the major constituent of

*Corresponding author: enjulima@gmail.com

a living organism, inadequate cooling with the formation of rigid crystalline ice can distort or destroy fine cellular structures or alter natural physiologic states. Ideally, one seeks to convert water into amorphous ice, which is controlled by the speed at which a sample is arrested into an ice matrix. When the cooling rate is slower than the critical rate at a given pressure, crystalline ice nucleation and propagation tend to prevail over the production of amorphous ice essential for preserving biological structures [24]. Figure 1(a) depicts two cryopreservation processes at different pressures. At ambient pressure (0.1 MPa), cryopreservation requires a cooling rate greater than 10^6 K per second to form amorphous ice in pure water [24]. Although biological samples contain a certain amount of natural cryoprotectants, it can be difficult to obtain the required high cooling rate in the interior of thick samples due to limited heat conduction. During high-pressure cryopreservation at around 200 MPa, the expansion of the ice

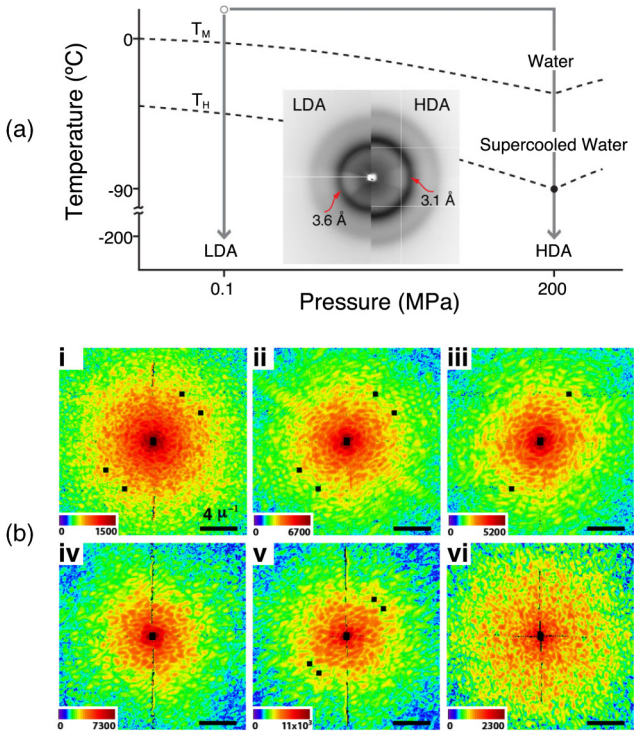

FIG. 1. (Color online) (a) A schematic of high-pressure and ambient-pressure cryopreservation in the water-ice phase diagram. T_M stands for the melting temperature of water and T_H stands for the homogeneous nucleation temperature, which is the low-temperature limit of supercooled water (adapted from Ref. [25]). The inset shows characteristic wide-angle x-ray scattering, measured from ~10-μm-thick ice layers, of LDA (low density amorphous ice) with peak scattering at 3.6 Å and HDA (high density amorphous ice) with peak scattering at 3.0–3.3 Å [26], of the current case at 3.1 Å. (b) Coherent x-ray diffraction patterns: (i–iii) from high-pressure-cryofixed *D. radiodurans* bacteria and (iv–vi) from ambient-pressure-cryofixed ones. The total exposure time is about one hour per data set. The color scales indicate the intensity in photon counts per second. The black scale bars (bottom right) in all images indicate spatial frequency $= 4\ \mu m^{-1}$. The missing data region behind the beam stop consists of 7×9 pixels. Oversampling ratios were estimated to be ~15 for panels i and vi and ~25 for the others (ii–v).

volume is suppressed and water may remain, down to near −90 °C, in a supercooled liquid state [25]. These changes in the physical properties of water reduce the critical cooling rate to 10^4 K per second, so that thick samples such as tissue sections can be cryopreserved with a reduced risk of crystalline ice formation [27].

To date, cryo XDM has utilized conventional ambient-pressure cryopreservation which has shown low phasing convergence and few imaging results [22,23]. It has even been questioned whether unstained biological specimens in a natural water contrast may be intrinsically too weak to produce high signal-to-noise–ratio diffraction patterns for successful imaging. Several factors, including parasitic scattering from beamline optics, partial coherence of x-rays, or crystalline ice contamination during measurements, contribute to the poor quality of diffraction patterns. One factor to consider, the initial ice condition, is often ruled out when the desirable amorphous ice state is confirmed by wide-angle x-ray scattering, as shown in the Fig. 1(a) inset. Although these measurements show amorphous ice on average, local ice conditions near the sample region cannot be determined by wide-angle x-ray scattering. This presents an uncertainty in cryo XDM performance, as discussed below.

While XDM bypasses the limitations of physical optics, it requires oversampling diffraction data for a successful phase retrieval [6,19]. This necessitates an isolated sample or spatially confined illumination and, in practice, either condition is difficult to obtain with frozen-hydrated specimens. Insufficient cryopreservation can induce ice imperfections in the close vicinity of specimens. These imperfections, which are structurally distinct from the homogenous amorphous ice, act as additional scatterers and can violate the isolated sample condition. Additionally, the illumination provided by coherent x-ray probes at modern synchrotron facilities is typically larger than the specimen size of a few microns. In our experiments, the probe beam is ~15 μm in size. Under these conditions, both cellular structures and the ice imperfections present within the illuminating area contribute to the diffraction pattern. However, since these signals are added coherently they cannot be subtracted reliably from each other, resulting in a reduced signal-to-noise ratio and a lower oversampling ratio in the diffraction data.

We carried out a comparison study of two methods of cryopreservation to probe the phasing dependance on local ice conditions. For the first time in cryo XDM, we applied high-pressure cryopreservation and compared it with conventional ambient-pressure cryopreservation in terms of local ice conditions and cryo XDM imaging performance.

A. Experimental details

D. radiodurans bacteria (ATCC® 13939™, Manassas, Virginia, USA), of a few microns in size, were selected as imaging samples. Bacteria were grown in a nutrient broth (ATCC®) at 30 °C and the culture medium was collected after 15 to 25 hours incubation at an optical density at 600 nm of 0.2 to 0.5. Prior to sampling bacteria cells with nylon loops, the culture medium was diluted into a glycerol-water solution yielding the final 10% glycerol concentration by volume. This

helped to reduce the surface tension of the water layer, formed without an underlying substrate, inside the nylon loops. Using a gas-charged high-pressure cryocooling procedure similar to that described by the Cornell group [28], sample loops inside a closed 2.4-mm-inner-diameter cylinder were pressurized, at room temperature, to 50 MPa within one to two minutes with He gas and then to 200 MPa during the next five minutes in the ESRF high-pressure apparatus [29]. Once the final pressure was reached, the sample loops were dropped into the cold bottom region of the cylinder, maintained near the liquid nitrogen temperature of $-196\,^{\circ}$C. The combination of adding 10% glycerol into the culture medium and the fast application of the initial 50 MPa pressure preserved the water layers during cryopreservation and obviated the need for a capillary shield or the oil coating used previously. For ambient-pressure cryopreservation, the loops were plunged into liquid ethane at atmospheric pressure. The performance of both cryopreservations in the current work was verified by wide-angle x-ray scattering, which showed a general state of amorphous ice [Fig. 1(a) inset].

Coherent diffraction measurements from the cryofixed bacteria were carried out at the ID10C beamline of the European Synchrotron Radiation Facility utilizing a cryogenic-gas sample environment in air and the beamline setup described previously [22]. A 10 μm pinhole, placed 50 cm upstream of the samples, provided spatially coherent x-rays of 8 keV at 10^9 photons per second and diffraction patterns from the samples were recorded on a Maxipix 2×2 chip detector [30] placed 3.54 meters from the samples. Three patterns were obtained from the high-pressure-cryofixed samples as shown in Fig. 1(b) (i–iii), and four from the ambient-pressure-cryofixed samples, of which three patterns are shown in Fig. 1(b) (iv–vi). The beamline configuration was identical for each measurement to allow a direct comparison of the data sets. We observed no signs of radiation damage while measuring signals down to a 25 nm half period.

B. Local ice conditions

We investigated the local ice conditions near the sample regions by small-angle x-ray scattering (SAXS), using a coherent x-ray beam of $\sim$15 μm in size at the sample plane. Figure 2(a) shows the power spectral densities measured from four ice layers that yielded the diffraction patterns in Fig. 1(b). Each spectral density is calculated from the average of 10 random sampling points per layer. The ambient-pressure ice layers (ii–iv) yielded higher x-ray scattering signals in the low spatial frequencies (SFs) up to $\sim$1 SF, compared to the ice layer (i) from high-pressure cryopreservation. This indicates the ambient-pressure ice layers have less spatial uniformity with an increased number of scattering elements larger than 0.5 μm. We deduce that these large scattering elements originate from ice crystals or density variations. However, it is experimentally challenging to measure crystalline ice rings *in situ* due to the limited coherent x-ray flux. Direct visualization of these ice layers was made by scanning and registering into pixels the total measured x-ray scattering intensity. From the scan images in Fig. 2(b), a high-pressure case (i) shows improved spatial uniformity of the ice over an area of several hundred microns, which is in agreement with the SAXS data.

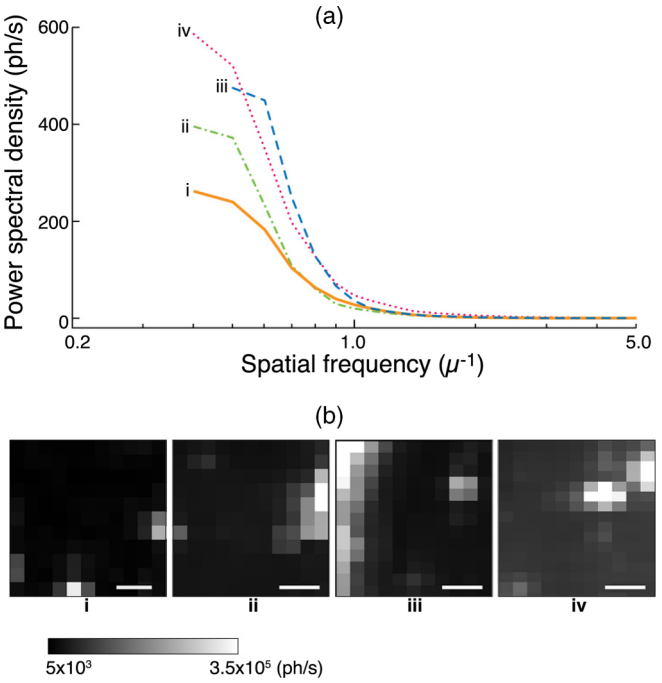

FIG. 2. (Color online) Coherent small-angle x-ray scatterings of ice layers. Panel (a) shows the power spectra, in photon counts per second, of ice signals, (i) from a high-pressure-cryofixed ice layer and (ii–iv) from ambient-pressure ones. The total exposure time for ten sampling points per spectrum was 30 s with an x-ray flux of 10^9 photons per second. The coherent scattering contrast images of corresponding ice layer is shown in panel (b). The area was scanned with 5–8 μm step size of the same x-ray illumination as in panel (a). The scale bars indicate 20 μm in size.

C. Reconstruction analysis

Reconstruction comparison was carried out between high-pressure and ambient-pressure cryofixed bacteria in terms of support estimation and final reconstruction images obtained. XDM reconstruction relies on the information of Fourier magnitude of the sample and a support of a spatial boundary, which in this case is the cell boundary. These two constraints are imposed iteratively until the lost phase information in a diffraction pattern is retrieved [9,10]. While x-ray diffraction measurements provide the Fourier magnitude of a sample directly, determining a sample support can be challenging without prior information, such as low-resolution optical images of a sample or symmetry information. This has been the main difficulty with frozen-hydrated specimens. Without *a priori* information, the sample support needs to be determined from the diffraction data alone by obtaining reproducible reconstructions of similar supports [13,31]. To provide a quantitative measure on a support estimation process between different bacteria specimens, we introduce image reproducibility **R** by calculating the averaged rate of image occurrence, which is defined as

$$\mathbf{R} = \frac{1}{S}\sum_i \left(\frac{\text{number of images per image set}_i}{N}\right) \quad \text{if } i > 0$$
$$= 0 \quad \text{if } i = 0$$

where N is the number of Shrinkwrap phase retrievals [31], an image set is a group of similar reconstructions obtained, and S is the total number of such image sets. The reproducibility defined here has a value of 1 when all phase seeds produce similar reconstructions, is equal to or less than 0.5 when half of the images are similar depending on S, and is 0 when none of the reconstructions are reproducible. We used 40 to 50 phase seeds ($N = 40$ to 50) per diffraction data set and similar reconstructions were visually selected based on their similarity of cell boundary. From high-pressure-cryofixed samples, reproducibility values of 0.2, 0.9, and 0.9 were obtained respectively, while four ambient-pressure-cryofixed samples yielded 0 for three samples and 0.9 for one. A support estimation was feasible, with a reproducibility of 0.2 and above, from the average of similar reconstructions by defining a spatial boundary at threshold intensity of 10% to 15% of the maximum pixel value.

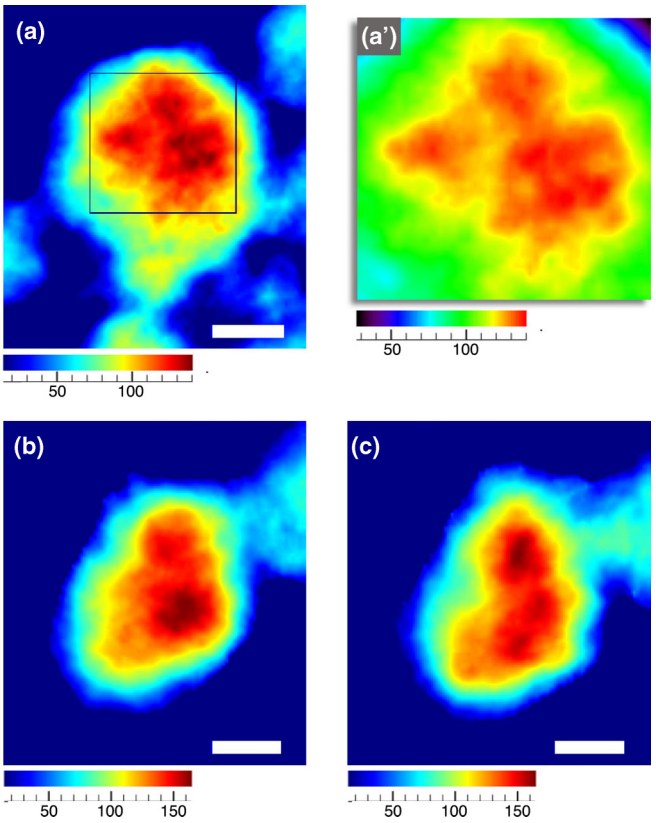

FIG. 3. (Color online) Reconstruction images of high-pressure-cryofixed *D. radiodurans* bacteria. The images show two bacteria samples: Panel (a′) is a magnified image of the sample from panel (a) in the region marked with the black square, and panels (b) and (c) are from the second bacteria, imaged at a 15-degree rotation from each other. Color scales display between 10% and 100% of maximum pixel value in each image. Here, the pixel values are normalized to photon counts per ten-minute exposure time. Sample sizes are ∼1.5 to 2 μm (the scale bars indicate 500 nm). Reconstruction images also show some low-density objects around samples, which are thought to be debris in the culture solutions. Each image is the average from 30 reconstruction trials with a total of 3000 [for panels (b) and (c)] and 6000 [for panel (a)] iterations.

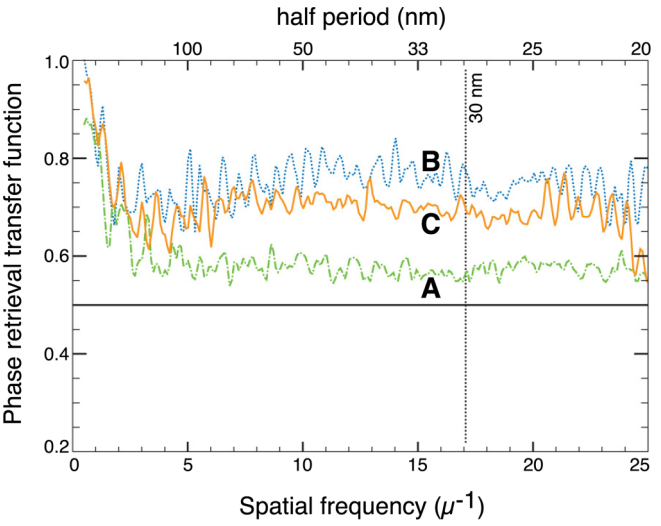

FIG. 4. (Color online) PRTF for high-pressure-cryofixed bacteria reconstructions. Curve "A" corresponds to Fig. 3(a) reconstruction, "B" for Fig. 3(b), and "C" for Fig. 3(c), respectively. Following the conservative measure for the resolution cutoff to be where PRTF falls below 0.5 [6], the resolutions of the reconstructions are estimated to be sub-30 nm.

For the final high-resolution images of the high-pressure cryofixed specimens, 30 reconstruction trials were carried out based on the supports calculated from reproducible images, using the difference map with phasing parameters of $\beta = 0.8$ or 1, $\gamma_1 = 1/\beta$, and $\gamma_2 = 1/\beta$ [10]. Figure 3 shows the resultant three reconstructions of high-pressure-cryofixed bacteria. The reconstructed images are proportional to the projected electron density variations of wet *D. radiodurans* along the direction of beam propagation, where x-ray dense regions in red are estimated to be nucleoid rich. Figure 3(a′) shows the inner cellular area from Fig. 3(a), which demonstrates the excellent hard-x-ray imaging sensitivity of cryo XDM with unstained, frozen-hydrated bacteria specimens. The estimated nucleoid-rich regions in these projection images are irregular in shape and do not resemble rings of packed nucleoid, which concurs with cryo EM images of sectioned, frozen-hydrated *D. radiodurans* [32]. The cell membranes or septa, however, are not visible in these two-dimensional views obtained at random orientations, as this would require three-dimensional imaging of bacteria cells to portray the complex cellular environments without projectional ambiguity. The resolutions of the three reconstructions are estimated to be sub-30 nm, based on phase retrieval transfer function (PRTF) [6] calculations shown in Fig. 4, while pixels have a spatial width of 25 nm.

With the ambient-pressure cryofixed samples, support estimations were not feasible with a reproducibility of 0 and no reconstructions resulted. While one of the data sets [Fig. 1(b)-(iv)] yielded low-resolution images with a reproducibility of 0.9 that led to sample supports, no high-resolution image was obtained at various support estimations. Imaging of several other ambient-pressure-cryofixed bacteria specimens was attempted at different x-ray energies of 7 keV, yet no imaging results were obtained with reproducibility values at 0. Ambient-pressure cryopreservation, using plunge freezing into liquid ethane as in the current work, is routinely practiced

in cryo electron microscopy of thin samples, mostly up to 0.5 μm thickness [33]. Our study shows that the conventional plunge freezing of microns-thick bacteria samples at ambient pressure yielded coherent x-ray diffraction data with low phasing convergence.

III. CONCLUSIONS

Scattering elements, such as ice crystals of varying size, randomly distributed outside of a sample can cause phasing difficulties, as discussed earlier. Yet a visual confirmation of ice quality at high resolution is challenging due to specific imaging requirements and limited resolution provided by x-ray optics. Small-angle x-ray scattering of ice regions $\sim$15 μm in size, on the other hand, provides an alternative from which one can deduce the level of ice scattering contamination in the diffraction pattern of a sample. With ambient-pressure cryopreservation, we observed increased background ice signals in the low spatial frequency range, and the corresponding reconstruction analysis showed low image reproducibility and poor imaging performance. Alternatively, high-pressure cryopreservation presented significantly lower background ice signals and allowed for high convergence imaging with multiple reconstructions of high-pressure cryofixed *D. radiodurans*. Our results indicate a phasing dependence of cryo XDM on the level of background ice signals and suggest high-background ice signals to be responsible for phasing difficulties. Other contributing factors may exist; however, their effects are considered to be less significant since the imaging comparison of the same bacteria strain was carried out under identical experimental conditions. The intrinsically weak x-ray scattering of biological specimens, especially in the frozen-hydrated state, challenges experimentalists, yet this appears not to be the primary cause of phasing difficulties. Further studies on ice conditions may allow identification of an acceptable range in which the background ice signals would still allow for a successful imaging. Identification of these conditions could significantly improve cryo XDM throughput.

Diffraction-based x-ray imaging at bright synchrotron x-ray sources is rapidly evolving as a means to visualize the internal structures of complex samples in biology and the physical sciences [34–36]. In this regard, we have demonstrated high-convergence imaging of cryo XDM on frozen-hydrated bacteria. Hydrated *D. radiodurans* cells were high-pressure-cryofixed at 200 MPa pressure into an amorphous ice layer that yielded diffraction with improved spatial uniformity. With accurate support estimation from reproducible low-resolution images, multiple two-dimensional reconstructions of *D. radiodurans* were obtained, revealing hydrated cellular environments at sub-30 nm resolution. A comparison with ambient-pressure-cryofixed bacteria studied under identical conditions showed higher-background ice scatter and increased irregularity, and a low success rate in the image reconstruction. Our findings demonstrate that phasing of cryo XDM depends on the ice quality of frozen-hydrated samples and suggest a possible cause for the earlier phasing difficulty. In addition, the high-pressure cryopreservation shown in the current work does not require cryo-sectioning of microns-to-tens-of-micron–thick specimens and enhances the fidelity of specimen preservation for x-ray imaging. The demonstrated high-convergence imaging of cryo XDM utilizing high-pressure cryopreservation may overcome current limitations in resolution and applicable sample thickness. This is promising for applications requiring high resolution imaging of relatively thick biological samples.

ACKNOWLEDGMENTS

We would like to thank the staff of ID10 and ID14 at the ESRF for their technical assistance at the beamlines and Huilin Li, Tao Wang, and EMBL Grenoble for providing help with the bacterial culture. Work at CHESS was supported by the NSF and NIH/NIGMS via NSF award DMR-1332208. The work at Brookhaven National Laboratory was supported by the BNL Laboratory-Directed Research and Development Program and the U.S. Department of Energy, Office of Science, under Contact No. DE-AC02-98CH10886.

[1] R. Feder, J. Costa, P. Chaudhari, and D. Sayre, Science **212**, 1398 (1981).
[2] P. Cloetens, R. Barrett, J. Baruchel, J. P. Guigay, and M. Schlenker, J. Phys. D: Appl. Phys. **29**, 133 (1996).
[3] M. D. de Jonge, C. Holzner, S. B. Baines, B. S. Twining, K. Ignatyev, J. Diaz, D. L. Howard, D. Legnini, A. Miceli, I. McNulty, C. J. Jacobsen, and S. Vogt, Proc. Natl. Acad. Sci. USA **107**, 15676 (2010).
[4] G. Schneider, P. Guttmann, S. Heim, S. Rehbein, F. Mueller, K. Nagashima, J. B. Heymann, W. G. Muller, and J. G. McNally, Nat. Methods **7**, 985 (2010).
[5] M. Lamvik, J. Microsc. **161**, 171 (1991).
[6] H. Chapman, A. Barty, S. Marchesini, A. Noy, S. Hau-Riege, C. Cui, M. Howells, R. Rosen, J. S. H. He, U. Weierstall, T. Beetz, C. Jacobsen, and D. Shapiro, J. Opt. Soc. Am. A **23**, 1179 (2006).
[7] Q. Shen, I. Bazarov, and P. Thibault, J. Synchrotron Radiat. **11**, 432 (2004).
[8] M. Howells, T. Beetz, H. Chapman, C. Cui, J. Holton, C. Jacobsen, J. Kirz, E. Lima, S. Marchesini, H. Miao, D. Sayre, D. Shapiro, J. Spence, and D. Starodub, J. Electron Spectrosc. Relat. Phenom. **170**, 4 (2009).
[9] J. R. Fienup, Appl. Opt. **21**, 2758 (1982).
[10] V. Elser, J. Opt. Soc. Am. A **20**, 40 (2003).
[11] J. Miao, K. Hodgson, T. Ishikawa, C. Larabell, M. Legros, and Y. Nishino, Proc. Natl. Acad. Sci. USA **100**, 110 (2003).
[12] D. Shapiro, P. Thibault, T. Beetz, V. Elser, M. Howells, C. Jacobsen, J. Kirz, E. Lima, H. Miao, A. M. Neiman, and D. Sayre, Proc. Natl. Acad. Sci. USA **102**, 15343 (2005).
[13] J. W. Miao, Y. Nishino, Y. Kohmura, B. Johnson, C. Y. Song, S. H. Risbud, and T. W. Ishikawa, Phys. Rev. Lett. **95**, 085503 (2005).

[14] M. A. Pfeifer, G. J. Williams, I. A. Vartanyants, R. Harder, and I. K. Robinson, Nature (London) **442**, 63 (2006).
[15] A. Barty, S. Marchesini, H. N. Chapman, C. Cui, M. R. Howells, D. A. Shapiro, A. M. Minor, J. C. H. Spence, U. Weierstall, J. Ilavsky, A. Noy, S. P. Hau-Riege, A. B. Artyukhin, T. Baumann, T. Willey, J. Stolken, T. van Buuren, and J. H. Kinney, Phys. Rev. Lett. **101**, 055501 (2008).
[16] Y. Nishino, Y. Takahashi, N. Imamoto, T. Ishikawa, and K. Maeshima, Phys. Rev. Lett. **102**, 018101 (2009).
[17] K. Giewekemeyer, P. Thibault, S. Kalbfleisch, A. Beerlink, C. M. Kewish, M. Dierolf, F. Pfeiffer, and T. Salditt, Proc. Natl. Acad. Sci. USA **107**, 529 (2010).
[18] S. Boutet *et al.*, Science **337**, 362 (2012).
[19] J. Miao, P. Charalambous, J. Kirz, and D. Sayre, Nature (London) **400**, 342 (1999).
[20] R. M. Glaeser and K. A. Taylor, J. Microsc. **112**, 127 (1978).
[21] S. Williams, X. Zhang, C. Jacobsen, J. Kirz, S. Lindaas, J. V. Hof, and S. S. Lamm, J. Microsc. **170**, 155 (1993).
[22] E. Lima, L. Wiegart, P. Pernot, M. Howells, J. Timmins, F. Zontone, and A. Madsen, Phys. Rev. Lett. **103**, 198102 (2009).
[23] X. Huang, J. Nelson, J. Kirz, E. Lima, S. Marchesini, H. Miao, A. M. Neiman, D. Shapiro, J. Steinbrener, A. Stewart, J. J. Turner, and C. Jacobsen, Phys. Rev. Lett. **103**, 198101 (2009).
[24] R. Dahl and L. A. Staehelin, J. Electron Microsc. Tech. **13**, 165 (1989).
[25] H. Kanno, R. J. Speedy, and C. A. Angell, Science **189**, 880 (1975).
[26] C. U. Kim, Y.-F. Chen, M. W. Tate, and S. M. Gruner, J. Appl. Crystallogr. **41**, 1 (2008).
[27] J. C. Gilkey and L. A. Staehelin, J. Electron Microsc. Tech. **3**, 177 (1986).
[28] C. U. Kim, R. Kapfer, and S. M. Gruner, Acta Crystallogr. D Biol. Crystallogr. **61**, 881 (2005).
[29] P. van der Linden, F. Dobias, H. Vitoux, U. Kapp, J. Jacobs, S. Mc Sweeney, C. Mueller-Dieckmann, and P. Carpentier, J. Appl. Crystallogr. **47**, 584 (2014).
[30] C. Ponchut, J. M. Rigal, J. Clément, E. Papillon, A. Homs, and S. Petitdemange, J. Instrum. **6**, C01069 (2011).
[31] S. Marchesini, H. He, H. Chapman, S. Hau-Riege, A. Noy, M. Howells, U. Weierstall, and J. Spence, Phys. Rev. B **68**, 140101 (2003).
[32] M. Eltsov and J. Dubochet, J. Bacteriol. **187**, 8047 (2005).
[33] *Electron Tomography - Methods for Three-Dimensional Visualization of Structures in the Cell*, 2nd ed., edited by J. Frank (Springer, New York, 2005).
[34] S. O. Hruszkewycz, M. V. Holt, C. E. Murray, J. Bruley, J. Holt, A. Tripathi, O. G. Shpyrko, I. McNulty, M. J. Highland, and P. H. Fuoss, Nano Lett. **12**, 5148 (2012).
[35] E. Lima, A. Diaz, M. Guizar-Sicairos, S. Gorelick, P. Pernot, T. Schleier, and A. Menzel, J. Microsc. **249**, 1 (2013).
[36] H. Jiang, R. Xu, C.-C. Chen, W. Yang, J. Fan, X. Tao, C. Song, Y. Kohmura, T. Xiao, Y. Wang, Y. Fei, T. Ishikawa, W. L. Mao, and J. Miao, Phys. Rev. Lett. **110**, 205501 (2013).